RSC Advances

Cite this: *RSC Adv.*, 2023, **13**, 11577

Metal-based-oxide nanoparticles assisted the *in vitro* culture growth of *Populus alba* as micronutrients: essential metabolic processes and genetic stability

Mohamed F. Ahmed,[a] Mostafa A. Ibrahim,[b] Ahmed S. Mansour,[cf]
Ahmed N. Emam,*[def] Ashraf B. Abd El-Razik[g] and Eman Tawfik[h]

The present study evaluates the *in vitro* culture growth rate of *Populus alba* upon using nano metal-based-oxides such as hematite (Fe_2O_3 NPs), zinc oxide (ZnO NPs), and manganese oxide (Mn_2O_3 NPs) nanoparticles as analogues of three primary micronutrients such as iron (Fe), zinc (Zn), and manganese (Mn), which exist in soil as micronutrients. Herein, the *in vitro* culture growth rate was investigated using three different concentrations (*i.e.*, 20, 40, and 60 mg L^{-1}) of as-prepared metal oxide nanoparticles compared to the control. In addition, the as-prepared nanoparticles have been prepared *via* the co-precipitation method. Furthermore, the physicochemical properties were investigated using transmission electron microscopy, Fourier transform infrared spectroscopy, X-ray diffraction, and dynamic light scattering techniques. Overall, a significant difference in the biomass production-related parameters such as fresh weight, shoot length, and root length was observed compared to the control upon the treatment with micronutrient-based nano-metal-oxides (*i.e.*, Mn_2O_3 > Fe_2O_3 > ZnO NPs, respectively). In addition, a significant increase in the root number of *Populus alba* plants upon their treatment with ZnO NPs was observed compared to other prepared nano-metal-oxides and the control. Also, a remarkable increase in the chlorophyll index was monitored upon the treatment with Fe_2O_3 NPs rather than the other commonly used Mn_2O_3 and ZnO NPs, respectively. Moreover, RAPD-PCR bioassays were applied, and the actual six primers showed a genetic variation percentage of 34.17%, indicating that *Populus alba* is highly genetically stable even in highly contaminated soil. As a result, our findings suggest an idea that indicates the ability to enhance the *in vitro* culture growth rate of *Populus alba* plants using metal oxide nanoparticles as analogous to essential micronutrients.

Received 20th September 2022
Accepted 4th April 2023

DOI: 10.1039/d2ra05941j

rsc.li/rsc-advances

1. Introduction

Heavy metals are still one of the most hazardous inorganic contaminants for water and soil composition due to their potential toxicity and bio-accumulative nature. In addition, extended human activities such as mining, chemical, and metal processing industries, and other allied industries significantly contribute to heavy metals in the environment at higher-than-normal levels.[1,2] Therefore, the development and survival of living organisms are threatened by the interference of these contaminants in the functioning of vital cellular components that exist in plant, animal, and human tissues.[2–4] Copper (Cu), lead (Pb), cadmium (Cd), mercury (Hg), nickel (Ni), cobalt (Co), and chromium (Cr) are examples of naturally abundant heavy metals. Except for Pb, Cd, and Hg, these elements are essential to organisms in minute amounts, but excessive amounts of these elements can be harmful.[5,6]

---

[a] *Horticulture Department, Faculty of Agriculture, Ain Shams University, P.O. Box 68, Hadayek Shobra, 11241, Cairo, Egypt*

[b] *Production and R&D Unit, NanoFab Technology Company, 6th October City, Giza, Egypt*

[c] *Department of Laser Applications in Meteorology, Chemistry and Agriculture, National Institute of Laser Enhanced Sciences (NILES), Cairo University, Cairo, Egypt*

[d] *Refractories, Ceramics and Building Materials Department, Advanced Materials Technology and Mineral Resources Research Institute, National Research Centre (NRC), El Bohouth St., Dokki, 12622 Cairo, Egypt. E-mail: ahmed.gsc.ndp@gmail.com; an.emam@nrc.sci.eg; Tel: +20 1018232249*

[e] *Nanomedicine & Tissue Engineering Lab., Medical Research Center of Excellence (MRCE), National Research Centre (NRC), Egypt*

[f] *Faculty of Postgraduate Studies for Nanotechnology, Cairo University, Zayed City, Giza, Egypt*

[g] *Genetics Department, Faculty of Agriculture, Ain Shams University, P.O. Box 68, Hadayek Shobra, 11241, Cairo, Egypt*

[h] *Botany and Microbiology Department, Faculty of Science, Helwan University, 11795, Cairo, Egypt*

Other heavy metals include Fe, Mn, and Zn, considered essential micronutrient elements for plants, animals, and other living organism.[7–9] However, toxic effects could be monitored upon uptake more than the plant's requirements and consequently harm the nutritional equilibrium in the soil.[10–12] Iron (Fe) is primarily involved in photosynthesis in plants. The availability of micronutrients to plant roots is affected by soil pH, with Fe being more readily available in soils with a low pH.[13–16] In addition, Fe is an essential component in the composition of heme proteins such as cytochromes, catalase, peroxidase, *e.g.*, hemoglobin, and iron-sulfur proteins like ferredoxin aconitase and superoxide dismutase (SOD).[17] At the same time, Zn aids in producing chlorophyll in plants. When the soil lacks Zn, the leaves darken, and plant growth is impeded.[18] In addition, Mn is a vital plant mineral nutrient involved in various physiological activities, including photosynthesis. Manganese shortages are common in sandy soils, organic soils with a pH above 6, and highly weathered tropical soils. Mn is easily transferred from root to shoot *via* the transpiration stream, but it is not easily remobilized to other organs *via* phloem once it reaches the leaves.[19]

Engineered nanomaterials have received significant attention due to their unique properties, which provide an opportunity to be used in several applications, especially in the agricultural sector.[20–23] Consequently, nanomaterials increase crop productivity through efficient regulation of micronutrient delivery to plants and targeted sites, ensuring that agrochemicals are used as little as possible, with efficient uptake of nutrients.[24,25] Such nano-fertilizers or nano-encapsulated nutrients may have qualities that are beneficial to crops, such as the on-demand release of nutrients and the controlled release of chemical fertilizers to regulate plant growth and accelerate target activity.[26–29]

Phytoremediation is a renewable technology that restores contaminated soil and water sources using natural or genetically modified plant species. In various review articles examining the principles, types, and mechanisms of the phytoremediation process, the advantages of low cost, environmental friendliness, and safety are highlighted.[30–33] Poplars are frequently used in phytoremediation because of their rapid growth, adaptability, and well-developed root system that reaches underground water and transports large amounts of water.[34] However, *P. alba* could not accumulate heavy metals like other hyper-accumulators, which can be overcome through high biomass production and, consequently, a relatively high amount of extracted metal per plant.[35–38] Particular white poplars, in particular, are interesting due to their high tolerance to arid conditions and their use in horticulture and landscaping, especially genotypes with a pyramidal tree shape.[39] The chemical composition of *Populus alba* wood varies according to the species and age of trees.[40] The following substances are present: mineral substances, extractives, cellulose, lignin, and holocellulose. Previous research found that trees cellulose and lignin content increases with age. The comparison of cellulose content in studied poplar wood, on the other hand, revealed that its content was unaffected by tree species, age, or growth environment.[40] While the content of extractives in poplar wood varied according to tree species and growth environment. Regardless of age, wood from *P. nigra* and *P. alba* contained less holocellulose than wood from *P. deltoides x maximowiczii* and *P. trichocarpa*. Finally, the lignin content of *Populus deltoides x maximowiczii* and *Populus trichocarpa* wood didn't vary with age and was comparable to that of 30 year-old Populus nigra wood. Furthermore, *P. alba* grows well in various soil and site conditions and is relatively resistant to climate changes such as drought, temperature, and salt.[41] It is primarily used in river lowland afforestation and is grown in specialised plantations to produce furniture logs, pallets, and other products.[42] Pelleri *et al.* discovered that *Populus alba* L. attains a commercially acceptable diameter after 9 to 10 years (30 cm).[43]

The *in vitro* culture of tree species offers a rapid instrument to produce the clonal planting stock. Still, it may also facilitate studies on the effects of elevated levels of heavy metals on plant performance and the selection of metal-tolerant genotypes.[38] In this regard, several reports have focused on the tolerance of *in vitro* cultured white poplars to heavy metals by monitoring the difference in their genotypes.[44–46] Based on developmental and molecular data, such systems could be sensitive and reliable for studying heavy metal stress responses of white poplars.[47]

Herein, we aim to investigate the *in vitro* culture growth assay of *Populus alba* upon the treatment with nano-oxide particle forms of each of Fe, Mn, and Zn (*e.g.*, Fe_2O_3, ZnO, and Mn_2O_3 NPs) as micronutrients through evaluation of growth parameters and photosynthetic index. In addition, test their genetic stability using RAPD-PCR techniques. The obtained results will help us track the phytoremediation activity of *Populus alba* (*P. alba*) *via* the plant's tolerance to growth in heavy metal contamination.

2. Experimental

2.1. Materials

Zinc sulfate heptahydrate ($ZnSO_4\cdot 7H_2O$, 99%), ferrous sulfate heptahydrate ($FeSO_4\cdot 7H_2O$, 98%), manganese sulfate ($MnSO_4$, 99%), and sodium hydroxide (NaOH, 98%) were used without any further purification. All the chemicals used were of analytical reagent grade, obtained from LOBA chemicals.

2.2. Preparation of nano-metal oxides for enhanced *in vitro* culture growth *P. alba* as phytoremediation of heavy metals

2.2.1. Preparation of iron oxide nanoparticles. Briefly, iron oxide (Fe_2O_3-NPs) nanoparticles were synthesized *via* the co-precipitation method as previously reported by Yang *et al.*[48] with slight modifications. Briefly, the iron salt precursor was mixed with deionized water under vigorous stirring for 10 min to ensure that all the ferrous salt dissolved at the concentration (1 M). In a 100 mL beaker, sodium hydroxide was prepared at a concentration of 2 M. Then, sodium hydroxide solution is added to the iron solution dropwise under constant stirring. After the complete addition of hydroxide solution, the reaction mixture is left for two hours. Finally, the black solution was washed repeatedly with deionized water to remove the excess hydroxides, keeping the pH of the slurry around 7, and dried at 50 °C overnight.

2.2.2. Preparation of zinc oxide nanoparticles. As previously reported, zinc oxide nanoparticles were prepared using the co-precipitation method.[49,50] Typically, sodium hydroxide aqueous solution was dropwise added slowly to an aqueous solution of zinc sulfate with a molar ratio of 1 : 2 under vigorous stirring for 12 h. The precipitate was centrifuged and washed with deionized water several times until pH (6.5–7). The resultant residue was dried in an oven at 80 °C and ground to a fine powder using a mortar. The powder was calcined for 2 hours at 300 °C.

2.2.3. Preparation of manganese dioxide nanoparticles. Manganese oxide nanoparticles have been prepared using co-precipitation, as reported by Kumar *et al.*[49] and Cherian *et al.*[47] Briefly, a freshly prepared 100 mL aqueous solution of 2 M NaOH was added drop by drop to 100 mL of 1 M $MnSO_4$. The solution was stirred continuously at 60 °C for 2 hours to precipitate the nanoparticles. The precipitate was separated from the reaction mixture, washed several times with deionized water, and dried in a hot air oven at 100 °C overnight.

2.3. Characterization

The morphological structure of the as-prepared nano-metal oxide particles (*e.g.*, Fe_2O_3, ZnO, and Mn_2O_3-NPs) was investigated using Transmission Electron Microscope (TEM) JOEL-JEM 2100 to investigate the micrograph of obtained samples under an operating voltage of 200 kV. X-ray diffraction (XRD) measurements have been carried out using a Bruker D8 advanced X-ray Powder Diffractometer operating with a Cu target with $K\alpha 1 = 1.54060$ Å, $K\alpha 2 = 1.5444$ Å, with 2θ step 4° and recorded at the range from 20° to 80°. In addition, the size distribution of as-prepared nanoparticles was measured by the Malvern Zeta-sizer Nano ZS instrument with a He/Ne laser (633 nm) at an angle of 173° using backscatter optics. Finally, Fourier-transform infrared spectroscopy (FT-IR) has been used to explore the chemical groups functionalized on their surfaces. The Brunauer–Emmet–Teller (BET) method was applied to obtain the surface area (S_{BET}) and non-local density functional theory (NL-DFT) for cylindrical pores was applied to evaluate the pore size distribution (PSD). N_2 physisorption experiments were carried out on surface area and pore size distribution analyser (BELSORP MAX). Prior to analysis, the samples were outgassed under high vacuum at 350 °C for 3 h. The adsorption/desorption isotherms were obtained at −196 °C allowing 4 min for equilibration between successive points. Textural properties were determined from the isotherms by using the BELMaster Data Analysis software. The pore volume was evaluated on the adsorption branch of the isotherm at $p/p_0 = 0.97$.

2.4. Plant materials and the *in vitro* culture with nano-metal oxide

Explants of *Populus alba* Lauche (*Populus alba* L.) nodal segments were cultured and acclimatized on Murashige and Skoog medium (MS medium) as previously reported.[51] Each nano-metal oxide (*i.e.*, Fe, Zn, Mn) used as a micronutrient was prepared at three different concentrations (*i.e.*, 20, 40, and 60 mg L^{-1}). These different concentrations were inoculated in MS jars separately. The nodal segments of *Populus alba* were cultured in these jars compared to the control. The culture was conducted at "Vitro Plant Labs". Each jar contains three explants. The culture conditions were conducted under white light with a light intensity of 38 μmol m^{-2} s^{-1}. After that, these cultures were incubated at 25 °C for four weeks, and the measurements were estimated.

2.5. Morphological measurements

This study measured seven morphological biometric parameters for all these treatments: plantlet fresh weight, shoot length, shoot number, root length, leaf number, number of roots, and rooting percentage. Seven to ten replicates for each parameter were measured for accurate mean results. The data obtained from all these parameters were applied to find out the relation among these different treatments.

2.5.1. Chlorophyll estimation. Chlorophyll index was measured using OPTI-SCIENCES (CCM-200 plus) to indicate the photosynthesis rate in response to the different nano-metal oxide uptake.

Fresh leaves from plantlets were used to measure chlorophyll a, b, carotenoids, and total pigmentation. They were determined in accordance with Metzner *et al.*[52] These leaves (0.5 g) were homogenised in 85% acetone, centrifuged, and transferred to a new tube. The extract was then measured using a colorimeter against a blank of 85% pure acetone at three different wavelengths (*i.e.*, 452, 645 and 664 nm). The concentrations of chlorophyll a, b, and carotenoids were calculated as g ml^{-1} using Metzner *et al.* equations;[52]

$$\text{Chl.a} = (10.3 \times A_{664}) - (0.918 \times A_{645})$$

$$\text{Chl.b} = (19.7 \times A_{645}) - (3.87 \times A_{664})$$

$$\text{Careteniods} = (4.3 \times A_{452}) \times ((0.0265 \times \text{Chl.a}) + (0.426 \times A\text{Chl.b}))$$

where A = absorbance at different wavelengths.

2.5.2. Estimation of nano-metal oxides particles contents in populus tissues. The content of nano-metal oxide particles (Fe_2O_3, ZnO, and Mn_2O_3 NPs) was estimated in the *P. alba* tissues in terms of metal ions such as Fe^{2+}, Zn^{2+}, and Mn^{2+} as previously reported[53,54] with slight modification. The plant tissues were dried in an oven at 80 °C for 48 h, ground well to powder, and fixed. The known weight of the samples (0.03 g) was digested with 5 mL of HNO_3 at 110 °C for 2 hours, cooled, and then boiled for 1 hour with 1 mL of H_2O_2. The clear digests were diluted to 50 mL with triple-deionized water.[55] The concentrations of the different nano-heavy metals as metal ions were estimated using Agilent 4200 MP-AES according to manufacturer instructions for mg L^{-1}.

2.6. DNA isolation and RAPD-PCR bioassay

The genomic DNA of *P. alba* from different treatments was isolated according to Lu *et al.*[56] According to Doyle and Doyle,[57]

Table 1 Primer data analysis of RAPD-PCR bioassay with Populus treatments

Name	Seq.	T_m	Total no. of bands	Polymorphic bands	Polymorphism (%)	Size range bp
Deca-12	5′-CTTGCCCACG-3′	38.5	4	0	0	509–792
Deca-13	5′-GTGGCAAGCC-3′	39	3	3	100	215–678
Deca-11	5′-ATCGGCTGGG-3′	39.3	5	1	20	135–559
Deca-7	5′-CCGCCCGGAT-3′	45	2	0	0	418–707
Deca-4	5′-CGTTGGCCCG-3′	44	4	1	25	194–566
Deca-10	5′-AGCCGGCCTT-3′	43.1	5	3	60	121–730
Total			23	8	34.17	

the total genomic DNA of *Populus alba* individuals was extracted using the CTAB method. Half gramme of leaves were mixed with 800 µl of 2% CTAB buffer and incubated at 65 °C for 45 minutes (vortex each 10 min). Centrifuge the tubes for 12 minutes at 12 000 rpm, then transfer the supernatant to new tubes with an equal volume of chloroform : isoamyl alcohol (24 : 1) and set for 3 minutes at room temperature. The tubes were then centrifuged (12 000 rpm per 10 min per 4 °C). The upper aqueous layer was then transferred to new Eppendorf tubes with 800 µl of absolute ice-cold ethanol added and stored overnight at −20 °C. After centrifuging the tubes to precipitate the DNA pellets, they were washed with ice-cold 70% ethanol. Finally, resuspend pellets in 50 µl of TE buffer and keep at −20 °C till applying RAPD-PCR.

A Random amplified polymeric DNA (RAPD-PCR) bioassay was applied using ten primers; only 6 of them gave clear, reproducible bands. The reaction mixture was prepared as follows; 12.5 µl of master mix (Bioline®), 1.5 µl of both forward and reverse primers; 2 µl genomic DNA, and diluted to 25 µl by adding 7.5 µl sterile ddH$_2$O. We performed the reaction program in the thermocycler Biometra® (Germany). The amplification process was performed using 35 cycles of 30 s at 95 °C, 30 s at the specific primer's melting temperature (T_m) (Table 1), and 1 min at 72 °C. PCR products were screened on a 1.4% (wt/vol) agarose gel (Agagel Mini; Biometra®). Gel images were analyzed with BioRad Quantity One (4.6.2) software using the method described by Williamson and Campbell[58] and Bio-Rad Laboratories (2005).

In random-amplified polymorphic DNA (RAPD) analyses a short primer is designed and added to a PCR reaction with the target DNA. RAPD is a PCR based technique for identifying genetic variation. The RAPD-PCR protocol consisted of an initial denaturing step of 2 min at 95 °C, followed by 45 cycles at 95 °C for 1 min (denaturation), 36 °C for 1 min (annealing of primers), and 72 °C for 2 min (extension). Cycling was concluded with a final extension at 72 °C for 4 min, and then held indefinitely at 4 °C.

2.7. Statistical analysis

This work's statistical analysis of the morphology, physiology and RAPD-PCR against different treatment with nano-metal oxide particle data was performed using Minitab 19 with the following analysis: descriptive analysis, general linear model, grouping by Tukey pairwise comparison, and correlation. A combined phylogenetic tree and principal component analysis (PCA) correlation plots were obtained using the Community Analysis Package (CAP software) to assess the relationship between all Populus treatments based on morphological, physiological, and molecular data. In addition, PCA is a software used to group the similar groups of treatment based on certain algorithm (Pearson correlation in this case).

3. Results

3.1. Preparation and characterization of nano-metal oxides particles

Metal-based oxide nanoparticles micronutrients including Fe$_2$O$_3$, ZnO, and Mn$_2$O$_3$ were prepared *via* co-precipitation methods.[48–50] In such cases, metal precursors such as FeSO$_4$, ZnSO$_4$, and MnSO$_4$ have been used, which chemically hydrolyse in an alkali medium to form metal-hydroxide. Then the metal-hydroxide precipitate was treated thermally to form metal-oxide nanoparticles. The formation mechanism for each of Fe$_2$O$_3$, ZnO, and Mn$_2$O$_3$ NPs was demonstrated as follows;

$$M - R + H_2O_{(hydration)} \rightarrow M_{(aq.)}{}^{+} + R^{-}_{(aq.)} \quad (1)$$

$$NaOH + H_2O_{(hydration)} \rightarrow Na^{+}_{(aq.)} + OH^{-}_{(aq.)} \quad (2)$$

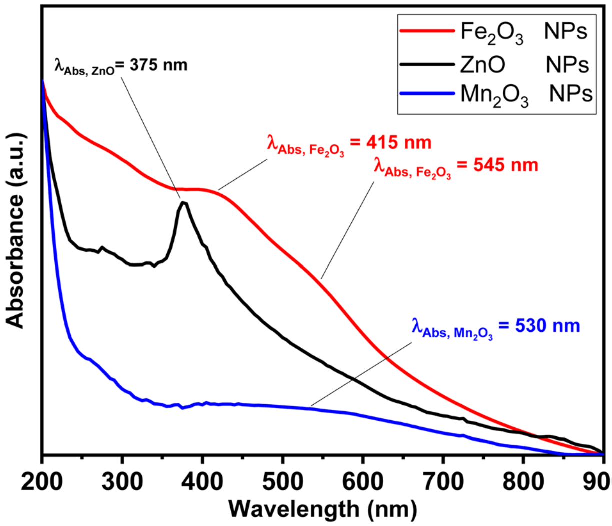

Fig. 1 Absorption spectra for ZnO (black line), Fe$_2$O$_3$ (red line) and Mn$_2$O$_3$ (blue line) nanoparticles.

$$x\mathrm{M}_{(\mathrm{aq.})}{}^{y+} + y\mathrm{OH}_{(\mathrm{aq.})}{}^{x-} \leftrightarrow \mathrm{M}_x\mathrm{OH}_y(\mathrm{ppt})\downarrow \xrightarrow[\text{calciation}]{\Delta} \mathrm{M}_x\mathrm{O}_y \text{ nanopowder} \tag{3}$$

where, M referred to metal cation in metal precursor (*i.e.*, Zn^{2+}, Fe^{3+} and Mn^{2+}, respectively) and R referred to anion in metal precursor (*i.e.*, $SO_4{}^{2-}$).

The photophysical properties such as UV-vis absorption spectra has been investigated as shown in Fig. 1. ZnO NPs exhibit a single narrow absorption band in UV region at 375 nm. While Fe_2O_3 showed a single and weak absorption band in a visible region at 415 nm and shoulder at 545 nm due to red colour characterized to hematite sample nature. Finally, a broad band at visible band at 530 nm.

The morphological structure has been confirmed *via* TEM and XRD measurements, as shown in Fig. 2 and 3, respectively. TEM micrographs showed that Fe_2O_3 NPs are quasi-spherical with a relatively narrow distribution. The average particle size was 20 ± 5 nm (Fig. 2a and b). While in the case of as-prepared ZnO-NPs, the average particle size was 30 ± 5 nm with a quasi-spherical shape (see Fig. 2c and d). Finally, the average particle size of Mn_2O_3 was 40 ± 10 nm, with agglomerated spherical nanoparticles in vesicles (see Fig. 2e and f).

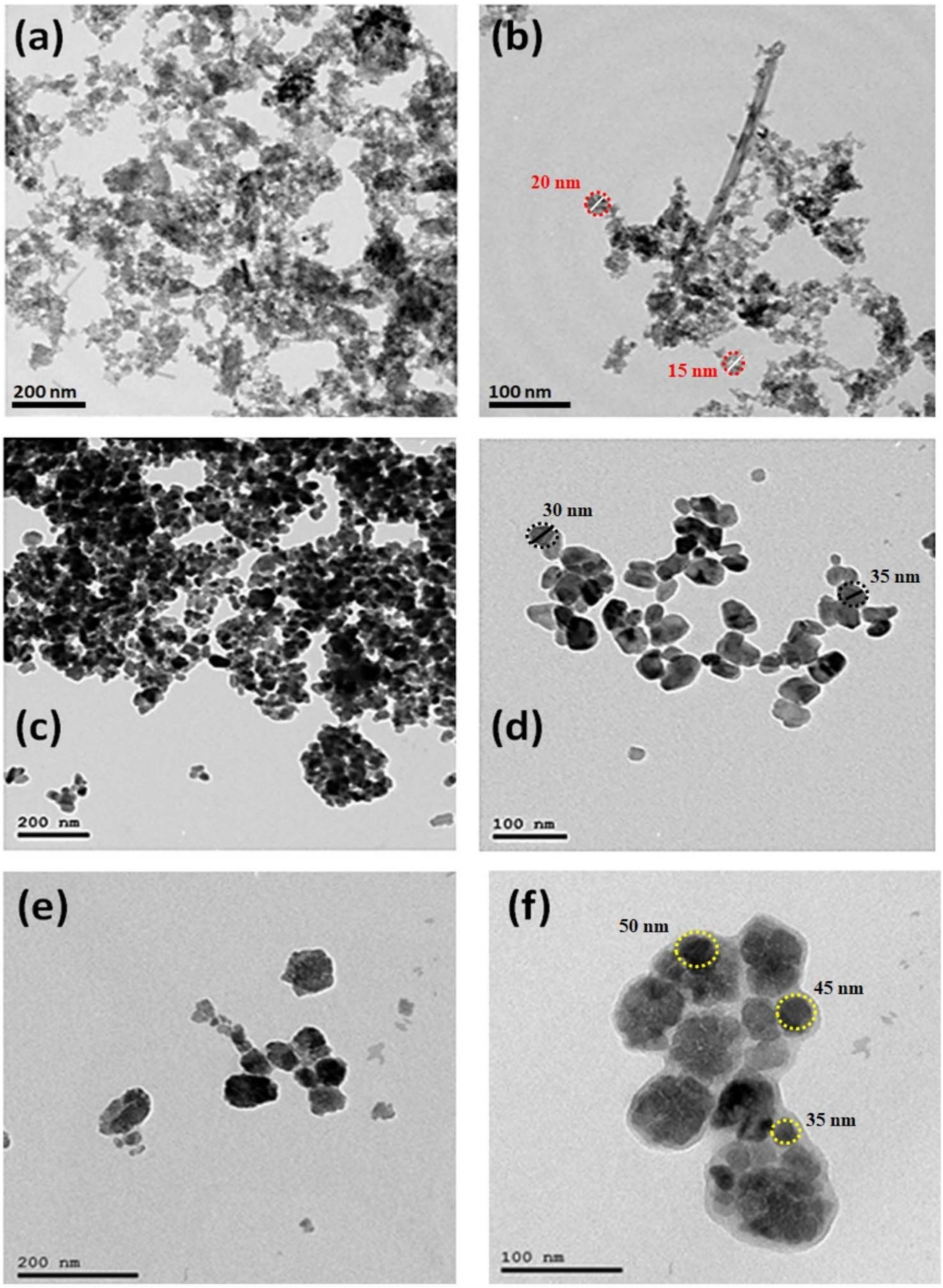

Fig. 2 TEM micrographs of Fe_2O_3 (a and b), ZnO (c and d) and Mn_2O_3 (e and f) nanoparticles at different magnification powers.

Furthermore, XRD measurements were carried out to investigate the crystallographic structure of as-prepared metal-based oxide nanoparticles of ZnO, Fe_2O_3, and Mn_2O_3-NPs, as shown in Fig. 3. XRD patterns of ZnO NPs indicated the formation of a hexagonal structure of ZnO nanoparticles (see Fig. 3a), where the three strongest lines have been obtained at 31.28°, 33.948°, and 35.81° due to the (100), (002), and (101) crystallographic plans of the hexagonal structure of ZnO NPs (*i.e.*, Zincite), as reported by ICCD-PDF No. 00-005-0664. In addition, the existence of five diffraction reflections at 47.14°, 55.93°, 62.33°, 67.47°, and 71.92° due to (102), (110), (103), (112), and (004) reflection plans for the hexagonal crystallographic structure of ZnO NPs. In addition, the average crystalline size of ZnO nanocrystals *via* Debye Sherer equation was about 7.98 ± 1.2 nm. Fig. 3b shows the XRD patterns of as-prepared hematite nanoparticles (*i.e.*, Fe_2O_3 NPs). Two of the strongest lines were observed at 32.6° and 35.16° due to (104) and (110) reflection plans of the rhombohedral crystallographic structure of hematite nanoparticles (*i.e.*, Fe_2O_3 NPs. See Fig. 3b). Moreover, another five diffraction patterns were at 40.35°,

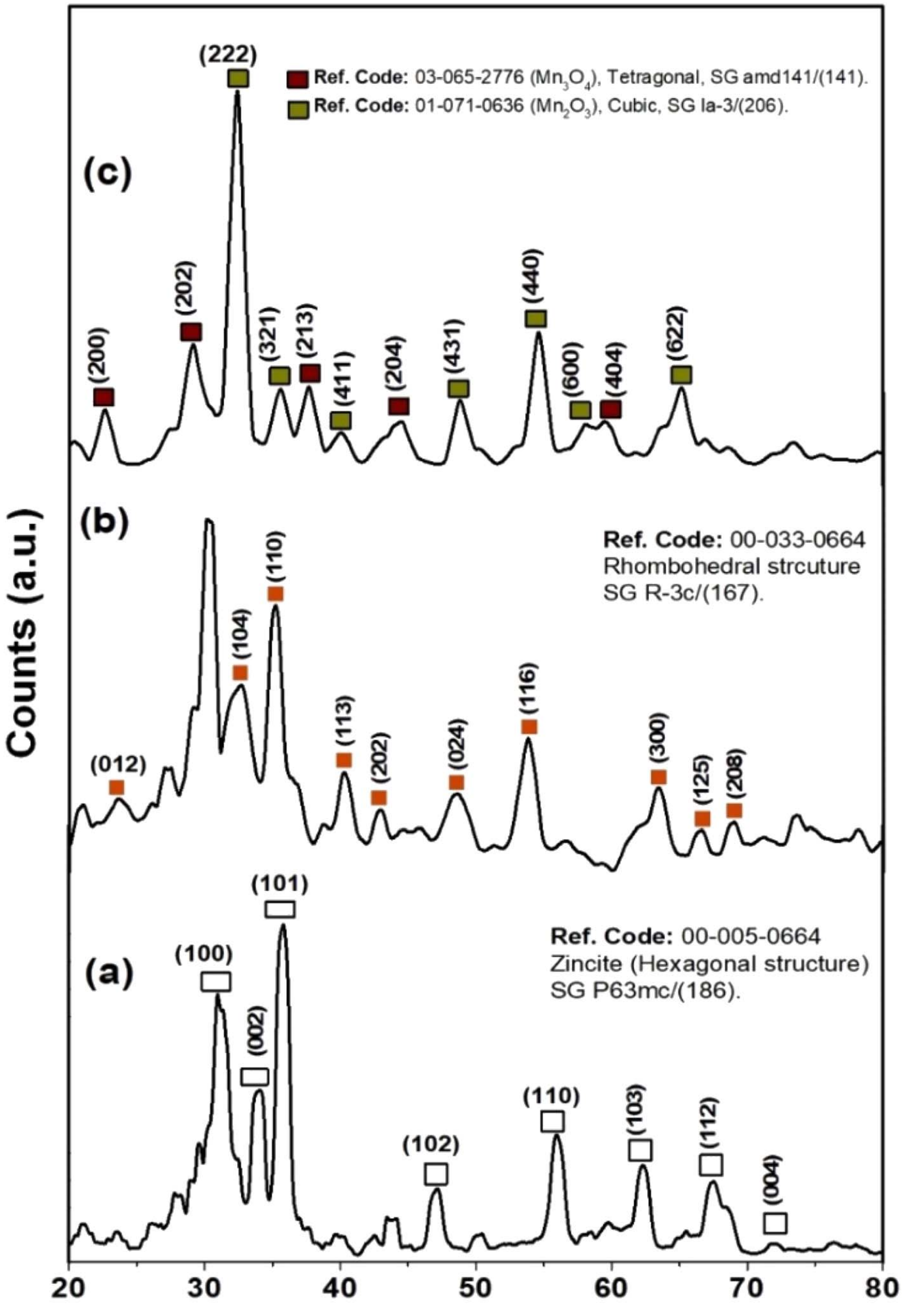

Fig. 3 XRD patterns of ZnO (a), Fe_2O_3 (b) and Mn_2O_3 (c) nanoparticles.

42.95°, 48.59°, 53.84°, and 63.48° due to (113), (202), (024), (116), and (300) reflection plans for the rhombohedral crystallographic structure of Fe_2O_3 NPs, respectively (see Fig. 3b). Also, the average crystalline size of Fe_2O_3 nanocrystals *via* Debye Sherer equation was about 6.22 ± 1 nm. XRD patterns of manganese oxide nanoparticles revealed a mixture of crystallographic reflection plans for both Mn(III) and Mn(IV) oxide nanoparticles (*i.e.*, Mn_2O_3 and Mn_3O_4 NPs), respectively. As depicted in Fig. 3c, Mn(III) oxide nanoparticles (Mn_2O_3 NPs) exhibited the dominant crystallographic structure with a cubic structure (see Fig. 3c). The two strongest lines of Mn_2O_3 were observed at 32.41° and 54.64°, corresponding to (222) and (440) reflection plans for the cubic structure of Mn_2O_3 NPs. Another four diffraction patterns accompanied these diffraction patterns were recorded at 35.56°, 40.1°, 48.89°, and 65.12°, corresponding to (321), (441), (431), and (622) reflection plans of Mn_2O_3 NPs. Furthermore, the minor phase Mn_3O_4 NPs, exhibit diffraction patterns at 22.62°, 29.17°, 37.66°, 44.55°, and 59.53° for (200), (202), (213), (204), and (404) reflection plans, respectively (see Fig. 3c), and the average crystalline size was about 6.17 nm.

Table 2 Colloidal properties of as-prepared nano-metal oxides particles

	Dynamic light scattering (DLS)		
Sample	Hydrodynamic diameter (HD, nm)	Polydispersity index (PDI)	Zeta potential (η, mV)
Fe_2O_3-NPs	232 ± 29.24	0.586	−6.96
Mn_2O_3-NPs	201 ± 143	0.585	+1.39
ZnO-NPs	129.1 ± 16.6	0.797	−14

In addition, the colloidal properties based on DLS and zeta potential measurements for Fe_2O_3, ZnO, and Mn_2O_3 nanoparticles were investigated, as shown in Fig. 4. The hydrodynamic particle size of as-prepared nanoparticles is remarkably increased, agreeing with their agglomeration presented in TEM micrographs, as shown in Fig. 2. This aggregation is due to its hydrophilic nature. In addition, the strength of the steric forces of the functional groups on the surface of nanoparticles and a steric interaction caused by the formation of a layer of water around the material.[59] In this regard, the hydrodynamic diameter (H_D) of Fe_2O_3 nanoparticles was about 232 ± 29.24 nm (see Fig. 4a and Table 2). In addition, Fe_2O_3 nanoparticles exhibit good dispersion in water, where the polydispersity index (PDI) is about 0.586.

Moreover, the zeta potential (η) of Fe_2O_3 nanoparticles was about −6.96 mV. The hydrodynamic particle size of Mn_2O_3 nanoparticles was smaller than Fe_2O_3, about 201 ± 143 nm. In addition, Mn_2O_3 nanoparticles exhibit a good dispersion in water, where the polydispersity index (PDI) is about 0.585 (see Fig. 4c and Table 2). Moreover, the zeta potential (η) of Mn_2O_3 nanoparticles is positively charged at +1.39 mV. Finally, ZnO NPs exhibited a smaller H_D than Fe_2O_3 and Mn_2O_3 NPs (see Fig. 4e and Table 2). The hydrodynamic particle size of ZnO NPs

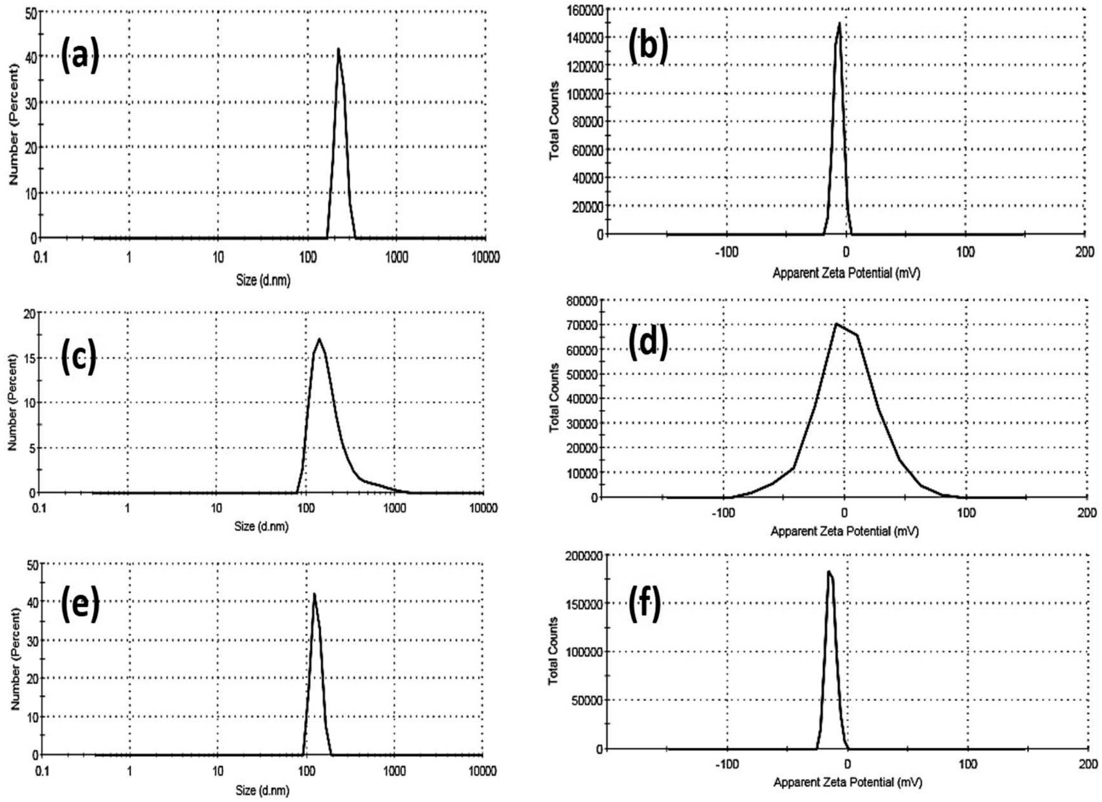

Fig. 4 DLS and zeta-potential data of Fe_2O_3 (a and b), ZnO (c and d) and Mn_2O_3 (e and f) nanoparticles.

was 129.1 ± 16.6 nm, and the polydispersity index (PDI) was about 0.797, indicating their fine dispersion in water.

Moreover, the ZnO nanoparticles' zeta potential (η) exhibits more electronegative behaviour at about −14 mV. Based on our findings, the size acquired by DLS, as shown in Table 2, is frequently larger than that obtained by TEM images, as shown in Fig. 2. DLS measurements are based on an intensity-based approach for solvated samples. The hydrodynamic diameter (H_D) is the size of the nanoparticle plus the liquid layer around the particle (*i.e.*, the relative humidity of the scattered particles). In contrast, TEM measurements are based on a number-based system dealing with dry samples under ultra-high vacuum conditions and calculating the projected surface area based on how much the incoming electrons passed through the sample.

Furthermore, the surface properties of the as-prepared metal-based oxide nanoparticles were explored *via* their FT-IR spectra, as shown in Fig. 5. The FT-IR spectrum of Fe_2O_3 NPs exhibited several absorption bands as follows (see Fig. 5a), considering the broadband for the –OH stretching vibration in the range of 3550–3100 cm^{-1}. Also, the absorption bands at 1640, 1430, and 1421 cm^{-1} are associated with the stretching vibration of the –C=O group and the bending vibration of adsorbed water, –CH group. The absorption band at 2890 cm^{-1} is attributed to the stretching vibration of the aliphatic saturated –CH group. The peaks for C–H and C–O bending vibrations are around 1157 and 1112 cm^{-1}, respectively. Furthermore, the bending vibration of the –C–O group is indicated by the absorption peak at 1060 cm^{-1}. While in the case of ZnO-NPs, the broadband for the –OH stretching vibration is in the range of 3420 cm^{-1}. Also, the absorption bands at 1640, 1430, and 1421 cm^{-1} are associated with the stretching vibration of the –C=O group and the bending vibration of adsorbed water, –CH group. The absorption band at 2925 cm^{-1} is attributed to the stretching vibration of the aliphatic saturated –CH group. The peaks for C–H and C–O bending vibrations are around 1157 and 1112 cm^{-1}, respectively. Furthermore, the bending vibration of the –C–O group is indicated by the absorption peak at 1060 cm^{-1}. The absorption band at 895 cm^{-1} is attributed to the strong bending vibration of –C=C– in vinylidene (see Fig. 5b). Finally, the FT-IR spectrum for the as-prepared Mn_2O_3 NPs depicted in Fig. 4c demonstrates that the broadband for the –OH stretching vibration is 3420 cm^{-1}. Also, the absorption bands at 1640, 1430, and 1421 cm^{-1} are associated with the stretching vibration of the –C=O group and the bending vibration of adsorbed water, –CH group. The absorption band at 2925 cm^{-1} is attributed to the stretching vibration of the aliphatic saturated –CH group. The peaks for C–H and C–O bending vibrations are around 1157 and 1112 cm^{-1}, respectively. Furthermore, the bending vibrations at 1060 and 895 cm^{-1} were attributed to the –C–O and –C=C– in vinylidene functional groups, respectively (see Fig. 5c). Based on the FTIR data, the –OH functional group that revealed water content/absorption onto the surfaces of the nanoparticles could improve the hydrophilicity of the as-prepared nano metal oxides in aqueous systems. In addition, improves the water uptake and maintains better water status under drought stress conditions and then improves the nutrients uptake such as nitrogen (N), and potassium (K),[60] and consequently improves seeds germination, plant growth, physiological functioning, photosynthetic efficiency, and hormonal activities.[60]

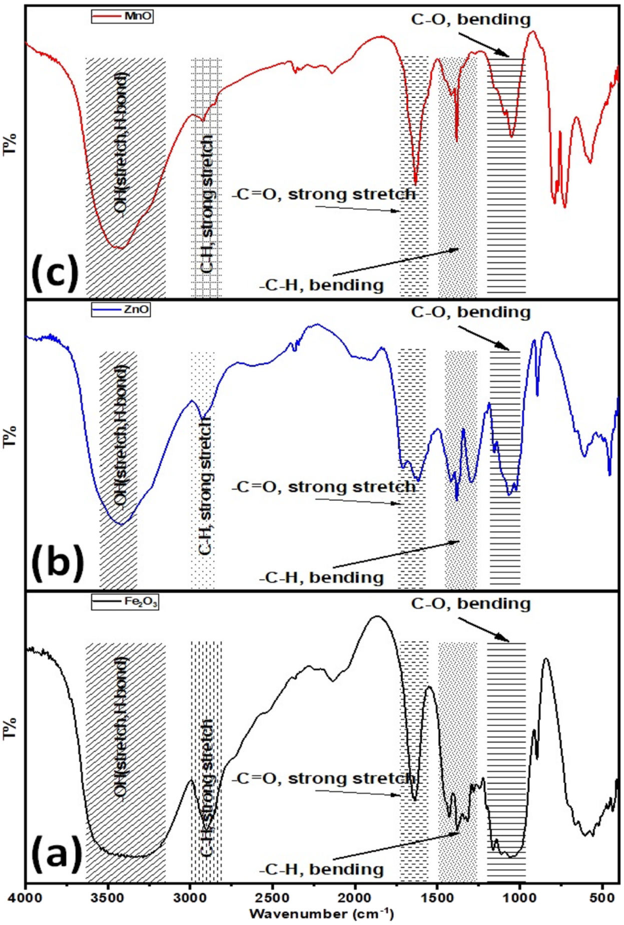

Fig. 5 FT-IR for Fe_2O_3 (a), ZnO (b) and Mn_2O_3 (c) nanoparticles.

Finally, N_2 adsorption/desorption technique was used in measuring the surface area and pore size distribution of the prepared nano compounds. Surface area parameters were evaluated for all the prepared samples using BET surface area measurements, as listed in Table 3. The surface area of ZnO nanoparticles was about 49.16 m^2 g^{-1}, which higher than both Mn_2O_3 and Fe_2O_3 with BET surface area value of 33.834 and 33.383 m^2 g^{-1}, respectively. In contrast Fe_2O_3 NPs showed a highest pore distribution compared to Mn_2O_3 and ZnO NPs. In addition, as-prepared metal oxides nanoparticles exhibited narrow pore size distributions, and capillary condensation steps on nitrogen adsorption isotherms as shown in Fig. 6a and b.

3.2. Morphological parameters and chlorophyll content

Seven morphological parameters, including one with a fixed rooting percentage of (100%) have been investigated for all treatments. The other six parameters varied and had significant differences in their treatment with three different levels of metal oxide nanoparticles compared to the control (Table 3). The chlorophyll index, reflecting the photosynthesis process,

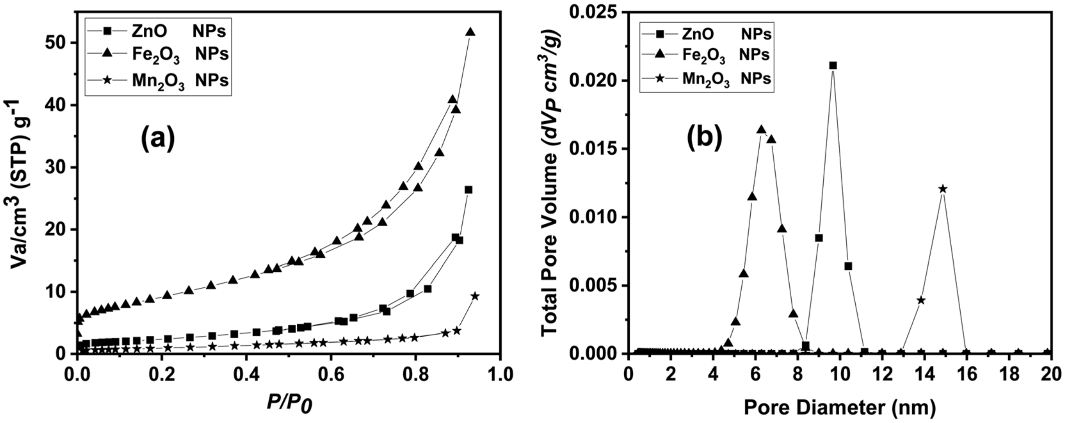

Fig. 6 BET data including (a) adsorption/desorption isotherm and (b) pore size distribution analysis for ZnO, Fe_2O_3 and Mn_2O_3 nanoparticles.

varied but had no significant difference (Table 4). Moreover, the correlation relationship among all the parameters (Table 5) illustrates that most of the parameters' ranges have positively affected each other, except rooting percentage, which negatively affected the other parameters in response to metal oxide nanoparticle treatments.

3.3. Estimation of metal oxide nanoparticles uptake in *Populus alba*

Populus alba treated with different nano-metal oxides. The metal uptake by *P. alba* was nearly the same with no significant differences (Table 6). These results confirm plant uptake of equivalent nano-heavy metals-based oxides. Hence, the estimated morphological and chlorophyll parameters are related to the type of nano-metal oxides besides the concentration.

3.4. DNA isolation and RAPD-PCR bioassay

The genetic stability of *Populus alba* treatments involving nano metal-based oxides, nanoparticles, and micronutrients has significant practical and commercial implications. In this study, we estimated the fingerprinting profiles of the regenerated culture by RAPD to confirm if the plantlets were

Table 3 BET surface area measurements

Sample	Surface area (S_{BET}), m^2 g^{-1}	BET analysis Total pore volume (V_p), cm^3 g^{-1}	Mean pore diameter (D), nm
ZnO NPs	49.1619	0.4087	17.844
Fe_2O_3 NPs	33.383	0.79839	9.4394
Mn_2O_3 NPs	33.834	0.14368	14.987

Table 4 Means of morphological and physiological parameters of *P. alba* L. in response to nano-metal oxides using Tukey pairwise comparison

	Fe_2O_3 NPs (mg L^{-1})			ZnO NPs (mg L^{-1})			Mn_2O_3 NPs (mg L^{-1})				
Treatment	20	40	60	20	40	60	20	40	60	Control	*P*-value
Fresh wt 'g'	0.210 ± 0.00115^d	0.191 ± 0.00115^e	0.178 ± 0.00115^g	0.145 ± 0.00153^h	0.135 ± 0.002^i	0.185 ± 0.003^f	0.223 ± 0.00115^c	0.261 ± 0.0025^b	0.292 ± 0.0025^a	0.189 ± 0.002^{ef}	0.00
Shoot length 'cm'	7.033 ± 0.058^b	6.766 ± 0.116^{bcd}	6.366 ± 0.153^e	5.566 ± 0.058^g	6.033 ± 0.058^f	6.566 ± 0.153^{cde}	7.033 ± 0.153^b	6.533 ± 0.058^{de}	7.966 ± 0.058^a	6.833 ± 0.058^{bc}	0.00
Shoot number	1.00 ± 0.00^b	1.00 ± 0.00^b	1.00 ± 0.00^b	1.00 ± 0.00^b	1.00 ± 0.00^b	1.00 ± 0.00^b	2.00 ± 0.00^a	2.00 ± 0.00^a	2.00 ± 0.00^a	1.00 ± 0.00^b	0.10
Leaf number	8.333 ± 0.577^c	9.00 ± 0.00^c	10.0 ± 0.00^c	8.667 ± 0.577c	9.0 ± 0.00^c	8.667 ± 1.155^c	14.33 ± 0.577^{ab}	15.66 ± 1.155^a	12.33 ± 1.155^b	9.00 ± 0.00^c	0.00
Root length 'cm'	4.133 ± 0.116^{cde}	4.433 ± 0.058^c	4.366 ± 0.153^{cde}	5.067 ± 0.058^b	4.067 ± 0.058^{de}	4.033 ± 0.058^e	8.033 ± 0.153^a	4.400 ± 0.173^{cd}	4.067 ± 0.116^{de}	5.133 ± 0.153^b	0.00
Root number	5.333 ± 0.577^d	7.00 ± 0.00^{bc}	7.00 ± 0.00^{bc}	7.667 ± 1.155^{ab}	6.00 ± 0.00^{cd}	8.667 ± 0.577^a	3.00 ± 0.00^e	5.00 ± 0.00^d	5.00 ± 0.00^d	5.667 ± 0.577^{cd}	0.00
Chl index	9.30 ± 8.20^a	10.90 ± 8.36^a	7.70 ± 5.49^a	3.333 ± 1.724^a	3.830 ± 1.80^a	4.330 ± 3.43^a	10.60 ± 7.02^a	5.130 ± 4.50^a	5.830 ± 4.87^a	5.630 ± 3.54^a	0.55

Table 5 Correlation among *Populus alba* different measured parameters in response to nano metal oxides treatments

	Fresh wt	Shoot length	Shoot no.	Leaf no.	Root length	Root no.
Shoot length	0.818					
Shoot no.	0.827	0.540				
Leaf no.	0.697	0.343	0.917			
Root length	0.060	0.068	0.412	0.432		
Root no.	−0.534	−0.492	−0.704	−0.634	−0.583	
Chlorophyll	0.131	0.170	0.092	0.031	0.198	−0.237

Table 6 Concentration of different nano-metal oxide uptake in *P. alba in vitro* culture

	Fe_2O_3 NPs (mg L^{-1})			ZnO NPs (mg L^{-1})			Mn_2O_3 NPs (mg L^{-1})				
Treatment	20	40	60	20	40	60	20	40	60	Control	*P*-value
Metal conc. 'ppm'	0.297^a	0.407^a	0.377^a	0.557^a	0.637^a	0.787^a	0.430^a	0.467^a	0.750^a	0.410^a	0.138^a

genetically stable or not. Ten random decamer-RAPD primers were tested for initial screening; only six primers gave clear and reproducible bands. The polymorphic bands ranged from 2 bands with the Deca-7 primer to 5 polymorphic bands with both the Deca-11 and Deca-10 primers (Table 1). These six primers produced 23 bands, with eight polymorphic bands, resulting in a total polymorphism percentage of 34.17% (see Fig. 7). The total molecular weights of all bands ranged from 121–792 bp. Fig. 8 shows a total phylogenetic tree that resulted from all the combined morphological parameters, chlorophyll index, and genetic variation. Fig. 9 showed the principal component analysis (PCA) plot, which showed the correlation between nano-metal oxide effects on the *P. alba* plant. The graph illustrated that responses to nano-Mn concentrations are separated, where control, nano-Fe, and nano-Zn are grouped. In addition, the Pearson correlation plot for the covariance ordination and

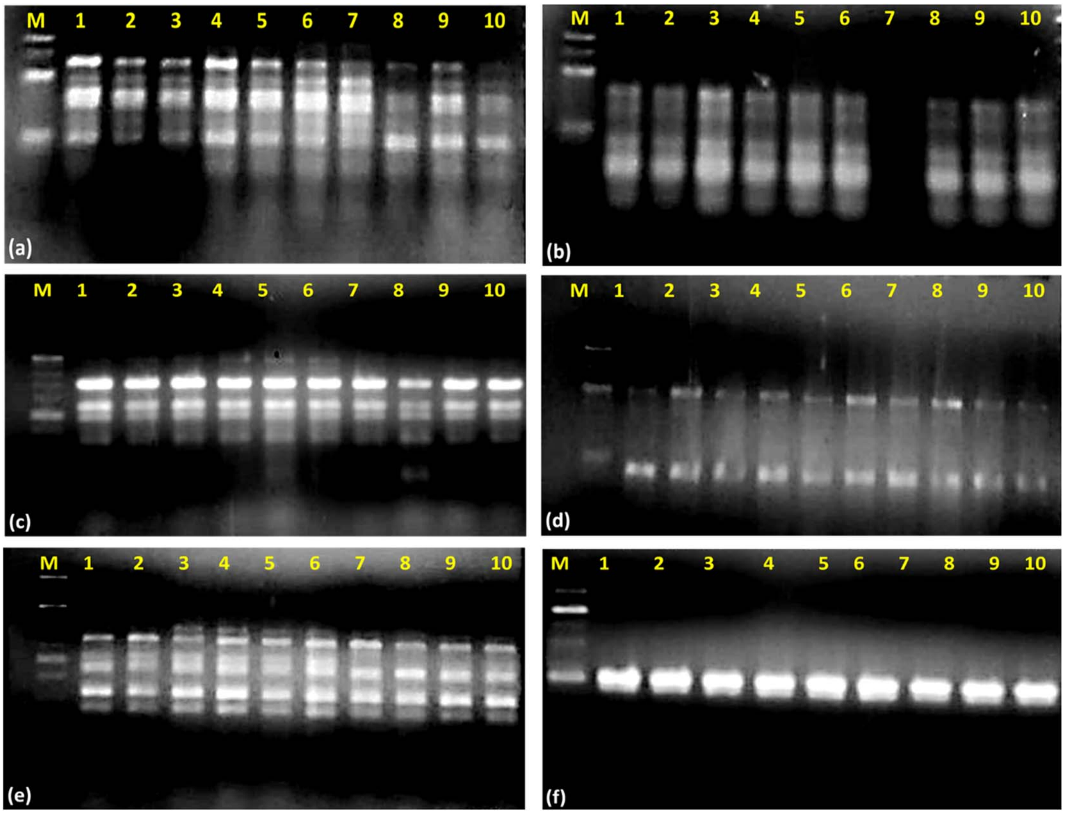

Fig. 7 Gel electrophoresis pattern of RAPD-PCR of *Populus alba* treated with different nano-heavy metals. (a) Deca-12; (b) Deca-13; (c): Deca-11; (d) Deca-7; (e) Deca-4; (f) Deca-10 (M: 100-base pair ladder; 1: 20 mg L^{-1} Fe; 2: 40 mg L^{-1} Fe; 3: 60 mg L^{-1} Fe; 4: 20 mg L^{-1} Zn; 5: 40 mg L^{-1} Zn; 6: 60 mg L^{-1} Zn; 7: 20 mg L^{-1} Mn; 8: 40 mg L^{-1} Mn; 9: 60 mg L^{-1} Mn; 10: control).

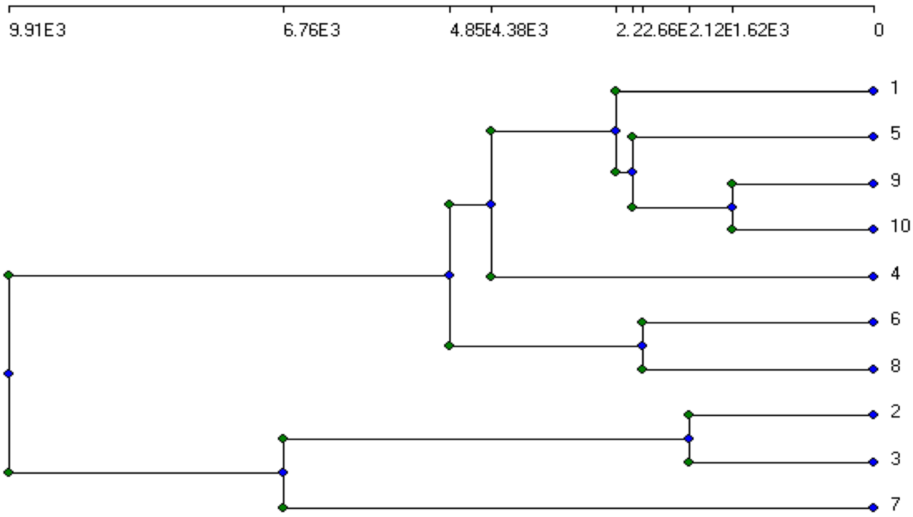

Fig. 8 Total phylogenetic tree of *Populus alba* treatments with different nano-heavy metals, resulted from all morphological parameters, chlorophyll index and genetic variation (1: 20 mg L^{-1} Fe; 2: 40 mg L^{-1} Fe; 3: 60 mg L^{-1} Fe; 4: 20 mg L^{-1} Zn; 5: 40 mg L^{-1} Zn; 6: 60 mg L^{-1} Zn; 7: 20 mg L^{-1} Mn; 8: 40 mg L^{-1} Mn; 9: 60 mg L^{-1} Mn; 10: control).

correlation based on morphology and physiology among different nano-metal oxides treatments of *Populus alba* has been illustrated in Fig. 10.

4. Discussion

Recently, looking for economic and eco-friendly soil heavy metal remediation techniques instead of conventionally used physicochemical techniques has become an urgent need. This is because biological techniques based on phytoremediation do not have any side effects on the soil ecosystem; they are economically viable compared to other traditionally used techniques.[33,61] The effect of *Populus alba* uptake on the nano-heavy metal micronutrients varied and was reflected in morphological and chlorophyll parameters. Some parameters were enhanced with exposure to heavy metal-based oxide nanoparticles-based micronutrients, while others were inhibited compared to control. The toxic effect of most heavy metals is caused by their bonding with –SH protein groups, leading to the inhibition of enzyme activity and compromising their structure. They also substitute essential elements in biomolecules, causing their deficiency.[62] Metal ion concentrations in the soil limit plant assimilation of essential micro-and macronutrients.[63]

The acclimatization of *P. alba* culture was performed by Ahmed *et al.*[51] and El-Sayed *et al.*[64] to obtain the best growth conditions. Gomes and co-workers explored the morphological, anatomical, and chlorophyll content of affected vegetation areas surrounding the mining company that produced heavy metals such as Zn, Cd, and Pb.[65] Moreover, Sadak and Bakry suggested using ZnO as an example of metal oxide-based

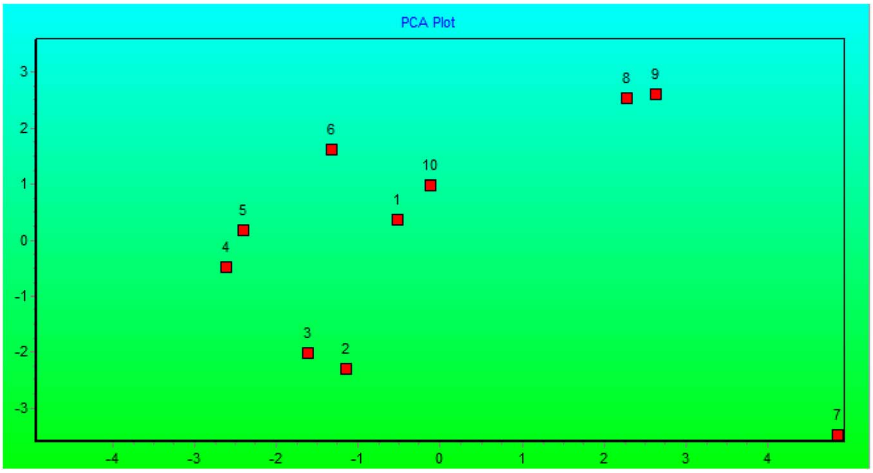

Fig. 9 PCA plot showing covariance ordination and correlation based on morphology, physiology and RAPD-PCR among different nano-metal oxides treatments of *Populus alba* (1: 20 mg L^{-1} Fe; 2: 40 mg L^{-1} Fe; 3: 60 mg L^{-1} Fe; 4: 20 mg L^{-1} Zn; 5: 40 mg L^{-1} Zn; 6: 60 mg L^{-1} Zn; 7: 20 mg L^{-1} Mn; 8: 40 mg L^{-1} Mn; 9: 60 mg L^{-1} Mn; 10: control).

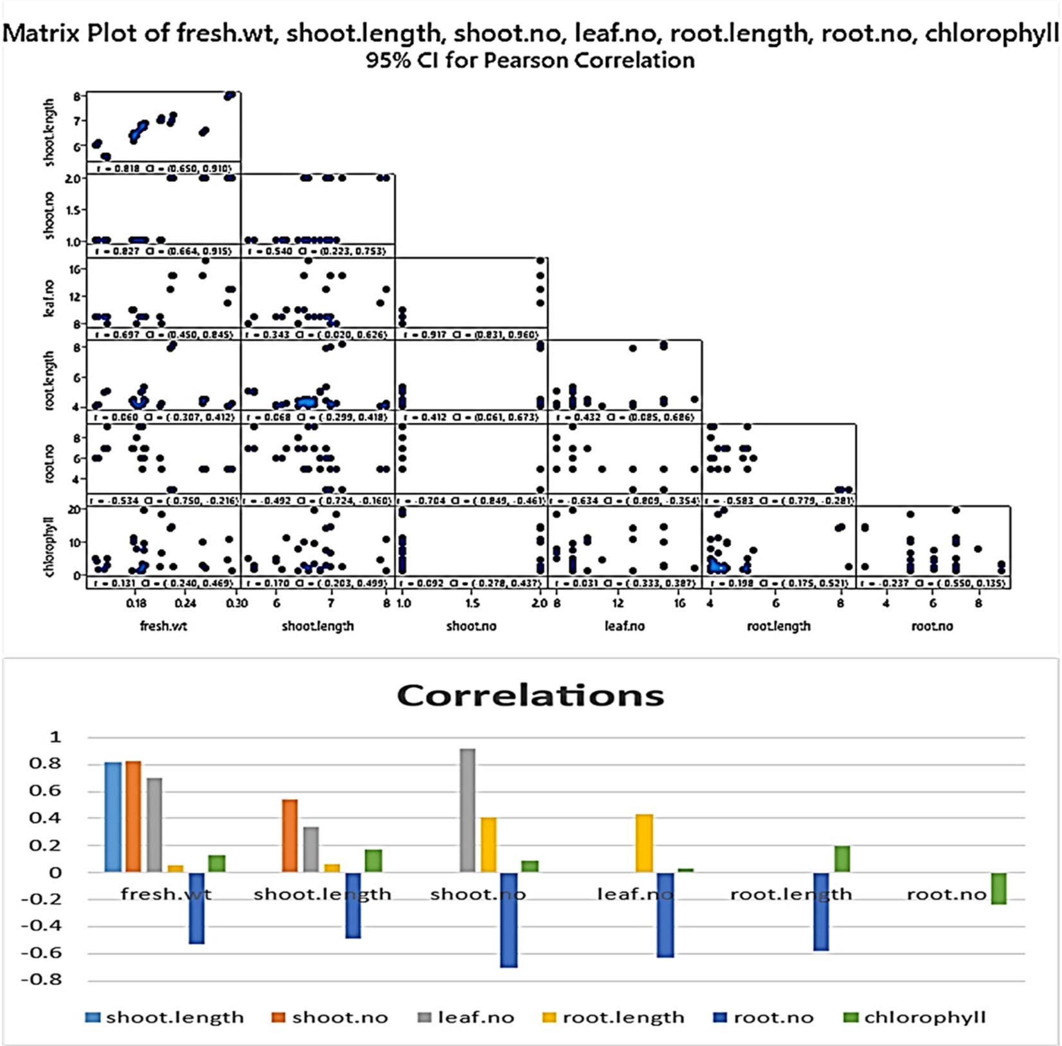

Fig. 10 Pearson plot showing covariance ordination and correlation based on morphology and physiology among different nano-metal oxides treatments of *Populus alba*.

nanomaterials rather than bulk forms in treating plants.[66] In such a study, ZnO-NPs exhibited an excellent effect and improved the biochemical, growth, and consequent biomass yield.

Our findings agreed with previous reports by Atteya *et al.*[67] and Gheith *et al.*,[68] respectively. In their studies, a remarkable increase in the biomass yield and plant growth parameters was observed upon the treatment of jojoba and maize with Zn precursors.[67,68] However, Prasad and co-workers proved that ZnO-NPs have a remarkable effect on enhancing peanut plant growth and that biomass yields are higher than ordinary Zn precursors such as $ZnSO_4$ at lower concentrations. This enhancement in peanut plant growth is attributed to the high adsorption of ZnO-NPs in the plant-based on their smaller size than $ZnSO_4$.[69] Finally, Tawfik and co-workers reported a significant increase in the growth parameters of *Atriplex halimus* upon treatment with ZnO-NPs in saline environments.[70] Furthermore, the efficiency of nanoparticles can vary with different genotypes and applications for various reasons, including differences in nanoscale size, the likelihood that these structures will lose their properties during plant physiological processes, and the properties of nanoscale metals.[71–73]

5. Conclusion

This study evaluated the *in vitro* propagation ability, photosynthetic pigment contents, and genetic variation of *P. alba* if the growth media includes metal-based oxide nanoparticles as a source of micronutrients such as ZnO, Fe_2O_3 and Mn_2O_3 NPs. These nanoparticles cause variation in growth due to changes in their physiological and biochemical activities, especially when the heavy metal involved plays a beneficial role in plant growth and development. The genetic variation in the DNA content of polluted *P. alba* individuals adapts the plant to tolerate and adapt to nano-metal contamination. Overall, a significant difference in the biomass production-related parameters such as fresh weight, shoot length, root length, and root number was observed compared to control upon the treatment with micronutrients in terms of Mn_2O_3 NPs as a source of Mn^{3+}. Whereas treatment with ZnO NPs showed a significant increase in the root number of *Populus alba* plants compared to control. Also, we monitored a remarkable increase in the chlorophyll index upon treatment with Fe_2O_3 NPs. Furthermore, RAPD-PCR bioassays demonstrated that metal oxide nanoparticles aided the *in vitro* culture of *Populus alba* and are highly genetically stable even in highly contaminated environments or soil.

Author contributions

Mohamed Fathy Ahmed; performed the agricultural experiments on the *P. alba*. Mostafa Ahmed Ibrahim and Ahmed Sadek Mansour; synthesis of nanomaterials. Ahmed Nabile Emam (corresponding author); synthesis and performing characterization experiments for metal oxide nanomaterials, data analysis & discussion, and writing/formulating and revising the manuscript. Ashraf Bakry Abd El-Razik; performing molecular genetic experiments. Eman Tawfik; conceptualization, contribution in performing and analysis of the agricultural and molecular genetics data.

Conflicts of interest

There are no conflicts to declare.

Acknowledgements

The authors thank Dr Aisha Mostafa and Dr Amal Farouk at the National Research Centre (NRC) X-Ray Crystallography Laboratory for performing XRD measurements of as-prepared metal oxide nanoparticles using the Bruker D8 advanced X-Ray Powder Diffractometer.

Notes and references

1 P. B. Tchounwou, C. G. Yedjou, A. K. Patlolla and D. J. Sutton, *Exp. suppl.*, 2012, **101**, 133–164.
2 H. Ali, E. Khan and I. Ilahi, *J. Chem.*, 2019, **2019**, 6730305.
3 M. Jaishankar, T. Tseten, N. Anbalagan, B. B. Mathew and K. N. Beeregowda, *Interdiscip. Toxicol.*, 2014, **7**, 60–72.
4 A. Asati, M. Pichhode and K. Nikhil, *Int. j. appl. innov. eng. manag.*, 2016, **5**, 56–66.
5 J. Briffa, E. Sinagra and R. Blundell, *Heliyon*, 2020, **6**, e04691.
6 I. Raskin, P. N. Kumar, S. Dushenkov and D. E. Salt, *Curr. Opin. Biotechnol.*, 1994, **5**, 285–290.
7 B. Singh and D. Schulze, *Nat. Educ. Knowl.*, 2015, **6**, 1.
8 D. G. Gomes, J. C. Pieretti, W. R. Rolim, A. B. Seabra and H. C. Oliveira, in *Advances in Nano-Fertilizers and Nano-Pesticides in Agriculture*, ed. S. Jogaiah, H. B. Singh, L. F. Fraceto and R. d. Lima, Woodhead Publishing, 2021, pp. 111–143, DOI: 10.1016/B978-0-12-820092-6.00005-7.
9 Z. Rengel, *J. Soil Sci. Plant Nutr.*, 2015, **15**, 397–409.
10 R. Djingova and I. Kuleff, in *Trace metals in the Environment*, Elsevier, 2000, vol. 4, pp. 137–185.
11 R. D. Reeves, *Phytoremediation of toxic metals: using plants to clean up the environment*, 2000.
12 H. Wintz, T. Fox and C. Vulpe, *Biochem. Soc. Trans.*, 2002, **30**, 766–768.
13 M. Becker and F. Asch, *J. Plant Nutr. Soil Sci.*, 2005, **168**, 558–573.
14 J. Morrissey and M. L. Guerinot, *Chem. Rev.*, 2009, **109**, 4553–4567.
15 G. R. Rout and S. Sahoo, *Rev. Agric. Sci.*, 2015, **3**, 1–24.
16 D. Neina, *Appl. Environ. Soil Sci.*, 2019, **2019**, 5794869.
17 A. Gautam and R. S. Dubey, *Molecular physiology of abiotic stresses in plant productivity*, 2018, pp. 256–290.
18 B. Hafeez, Y. Khanif and M. Saleem, *J. Exp. Agric. Int.*, 2013, 374–391.
19 J. F. Loneragan, in *Manganese in soils and plants*, Springer, 1988, pp. 113–124.
20 H. Chhipa, *Methods Microbiol.*, 2019, **46**, 115–142.
21 M. Usman, M. Farooq, A. Wakeel, A. Nawaz, S. A. Cheema, H. ur Rehman, I. Ashraf and M. Sanaullah, *Sci. Total Environ.*, 2020, **721**, 137778.
22 H. Chemingui, M. Smiri, T. Missaoui and A. Hafiane, *Bull. Environ. Contam. Toxicol.*, 2019, **102**, 477–485.
23 M. Naderi and A. Abedi, *J. Nanotechnol.*, 2012, **11**, 18–26.
24 D. Mishra and P. Khare, in *Sustainable Agriculture Reviews 50: Emerging Contaminants in Agriculture*, ed. V. Kumar Singh, R. Singh and E. Lichtfouse, Springer International Publishing, Cham, 2021, pp. 235–257, DOI: 10.1007/978-3-030-63249-6_9.
25 N. Sarkar, S. Chaudhary and M. Kaushik, in *Plant-Microbes-Engineered Nano-particles (PM-ENPs) Nexus in Agro-Ecosystems: Understanding the Interaction of Plant, Microbes and Engineered Nano-particles (ENPS)*, ed. P. Singh, R. Singh, P. Verma, R. Bhadouria, A. Kumar and M. Kaushik, Springer International Publishing, Cham, 2021, pp. 153–163, DOI: DOI: 10.1007/978-3-030-66956-0_10.
26 P. Zhang, Z. Guo, S. Ullah, G. Melagraki, A. Afantitis and I. Lynch, *Nat. Plants*, 2021, **7**, 864–876.
27 K. Sampathkumar, K. X. Tan and S. C. J. Loo, *iScience*, 2020, **23**, 101055.
28 M. C. DeRosa, C. Monreal, M. Schnitzer, R. Walsh and Y. Sultan, *Nat. Nanotechnol.*, 2010, **5**, 91.
29 R. Nair, S. H. Varghese, B. G. Nair, T. Maekawa, Y. Yoshida and D. S. Kumar, *Plant Sci.*, 2010, **179**, 154–163.
30 E. L. Arthur, P. J. Rice, P. J. Rice, T. A. Anderson, S. M. Baladi, K. L. Henderson and J. R. Coats, *Crit. Rev. Plant Sci.*, 2005, **24**, 109–122.
31 S. Parmar and V. Singh, *J. Plant Sci. Res.*, 2015, **2**, 135.
32 M. Laghlimi, B. Baghdad, H. El Hadi and A. Bouabdli, *Open J. Ecol.*, 2015, **5**(8), 375–388.
33 M. M. Al-Khazan and R. M. Al-Zlabani, *Egypt. J. Exp. Biol. (Bot.)*, 2019, **15**, 87–97.
34 E. W. Aitchison, S. L. Kelley, P. J. Alvarez and J. L. Schnoor, *Water Environ. Res.*, 2000, **72**, 313–321.
35 I. Pulford and C. Watson, *Environ. Int.*, 2003, **29**, 529–540.
36 M. Laghlimi, B. Baghdad, H. El Hadi and A. Bouabdli, *Open J. Obstet. Gynecol.*, 2015, **5**, 375.
37 W. T. Liu, J. C. Ni and Q. X. Zhou, 2013.
38 S. Di Lonardo, M. Capuana, M. Arnetoli, R. Gabbrielli and C. Gonnelli, *Environ. Sci. Pollut. Res.*, 2011, **18**, 82–90.

39 B. Kovačević, S. Orlović, S. Rončević and D. Miladinović, *Acta Hortic.*, 2010, **885**, 197–202.

40 D. Krutul, T. Klosinska, A. Antczak, M. Drozdzek, A. Radomski and J. Zawadzki, *Ann. WULS Forest. Wood Technol.*, 2019, **105**, 125–132.

41 J. Richardson, J. Isebrands and J. Ball, *Poplars and willows: Trees for society and the environment*, pp. 92–123, 2014.

42 D. I. Dickmann and J. Kuzovkina, in *Poplars and willows: Trees for society and the environment*, CABI, Wallingford UK, 2014, pp. 8–91.

43 F. Pelleri, S. Ravagni, E. Bianchetto and C. Bidini, *Ann. Silvic. Res.*, 2013, **37**(1), 13–21.

44 I. Kališová-Špirochová, J. Punčochářová, Z. Kafka, M. Kubal, P. Soudek and T. Vaněk, *Water, Air, Soil Pollut.: Focus*, 2003, **3**, 269–276.

45 K. Bojarczuk, *Pol. J. Environ. Stud.*, 2004, **13**, 115–120.

46 M. Katanic, A. Pilipovic, S. Orlovic, B. Krstic, B. Kovacevic and S. Pekec, 2008.

47 E. Cherian, A. Rajan and G. Baskar, *Int. J. Mod. Sci. Technol.*, 2016, **1**(1), 17–22.

48 X.-C. Yang, Y.-L. Shang, Y.-H. Li, J. Zhai, N. R. Foster, Y.-X. Li, D. Zou and Y. Pu, *J. Nanomater.*, 2014, **2014**, 740856.

49 A. Shoba, B. Kavitha, H. Aswathaman, H. Ganesan and N. S. Kumar, *Mater. Today: Proc.*, 2022, **48**, 521–526.

50 V. Koutu, L. Shastri and M. M. Malik, *Mater. Sci.*, 2016, **34**, 819–827.

51 M. Hewidy, A. M. Hosni, A. Abdel Razik, M. F. Ahmed and M. Bahnasy, *Arab. Univ. J. Agric. Sci.*, 2019, **27**, 2273–2290.

52 H. Metzner, H. Rau and H. Senger, *Planta*, 1965, **65**, 186–194.

53 R. A. Isaac and J. D. Kerber, *Instrumental methods for analysis of soils and plant tissue*, 1971, pp. 17–37.

54 Z.-Y. Hseu, *Bioresour. Technol.*, 2004, **95**, 53–59.

55 S. Shirani Bidabadi, *Int. J. Phytorem.*, 2020, **22**, 1259–1268.

56 Y. Lu, S. Chanroj, L. Zulkifli, M. A. Johnson, N. Uozumi, A. Cheung and H. Sze, *Plant Cell*, 2011, **23**, 81–93.

57 J. J. Doyle, *Focus*, 1990, **12**, 13–15.

58 A. M. Campbell, *Am. Biol. Teach.*, 1997, **59**, 164–170.

59 W. Marimón-Bolívar and E. E. González, *Dyna*, 2018, **85**, 19–26.

60 A. Rasheed, H. Li, M. M. Tahir, A. Mahmood, M. Nawaz, A. N. Shah, M. T. Aslam, S. Negm, M. Moustafa, M. U. Hassan and Z. Wu, *Front. Plant Sci.*, 2022, **13**, 1–15.

61 M. T. Gómez-Sagasti, I. Alkorta, J. M. Becerril, L. Epelde, M. Anza and C. Garbisu, *Water, Air, Soil Pollut.*, 2012, **223**, 3249–3262.

62 F. Van Assche and H. Clijsters, *Plant, Cell Environ.*, 1990, **13**, 195–206.

63 J. Oleksyn, P. Karolewski, M. Giertych, A. Werner, M. Tjoelker and P. Reich, *Trees*, 1996, **10**, 135–144.

64 I. M. El-Sayed, S. A. Shaaban, L. S. Taha and M. H. Mahgoub, *Plant Arch.*, 2019, **19**, 2655–2663.

65 M. P. Gomes, T. C. L. L. d. S. Marques, M. d. O. G. Nogueira, E. M. d. Castro and Â. M. Soares, *Sci. Agric.*, 2011, **68**, 566–573.

66 M. S. Sadak and B. A. Bakry, *Bull. Natl. Res. Cent.*, 2020, **44**, 98.

67 A. K. Atteya, E. A. Genaidy and H. A. Zahran, *Biosci. Res.*, 2018, **15**, 1528–1541.

68 E.-S. M. S. Gheith, M. M. Shafik, O. Z. El-Badry and B. M. A. Kareem, *Biosci. Res.*, 2018, **15**, 54–59.

69 T. Prasad, P. Sudhakar, Y. Sreenivasulu, P. Latha, V. Munaswamy, K. R. Reddy, T. Sreeprasad, P. Sajanlal and T. Pradeep, *J. Plant Nutr.*, 2012, **35**, 905–927.

70 M. Tawfik, G. Bakhoum, S. Sadak Mervat and M. Kabesh, *Bull. Natl. Res. Cent.*, 2017, **41**, 286–305.

71 O. B. Nalci, H. Nadaroglu, A. H. Pour, A. A. Gungor and K. Haliloglu, *Plant Cell, Tissue Organ Cult.*, 2019, **136**, 269–277.

72 Z. Wang, L. Xu, J. Zhao, X. Wang, J. C. White and B. Xing, *Environ. Sci. Technol.*, 2016, **50**, 6008–6016.

73 W.-M. Lee, Y.-J. An, H. Yoon and H.-S. Kweon, *Environ. Toxicol. Chem.*, 2008, **27**, 1915–1921.